Soft Matter

PAPER

View Article Online
View Journal | View Issue

Cite this: *Soft Matter*, 2014, **10**, 6713

Defect structures and ordering behaviours of diblock copolymers self-assembling on spherical substrates

Liangshun Zhang,* Liquan Wang and Jiaping Lin*

Received 1st June 2014
Accepted 25th June 2014

DOI: 10.1039/c4sm01180e

www.rsc.org/softmatter

One of the main differences of ordered structures constrained on curved surfaces is the nature of topological defects. We here explore the defect structures and ordering behaviours of both lamellar and cylindrical phases of block copolymers confined on spherical substrates by the Landau–Brazovskii theory, which is numerically solved by a highly accurate spectral method with a spherical harmonic basis. For the cylindrical phase, isolated disclinations and scars are generated on the spherical substrates. The number of excess dislocations in a scar depends linearly on the sphere radius. The defect fraction characterizing the ordering dynamics decays exponentially. The scars are formed from the isolated disclinations *via* mini-scars. For the lamellar phase, three types of defect structures (hedgehog, spiral and quasi-baseball) are identified. The disclination annihilation is the primary ordering mechanism of the lamellar phase.

1 Introduction

As a result of a large number of theoretical and experimental studies, the bulk phase behaviours of linear diblock copolymers have been well mapped out.[1,2] However, newer technological applications of copolymers for nanolithography, nanosize bioreactors and drug delivery vehicles necessitate tailoring their morphologies.[3–6] Confining the block copolymers on substrates introduces geometric frustration in systems, and allows materials to self-assemble into new nanostructures that are very different from their bulk morphologies. The simple case of block copolymers under confinement is the one-dimensional (1D) confined system, in which the block copolymers are placed between two flat parallel walls. One can observe structures, such as perforated lamellae, parallel or perpendicular lamellae and cylinders.[7–9] The two-dimensional (2D) and three-dimensional (3D) confinements are realized by putting copolymers into cylindrical nanopores and spherical cavities, respectively. A rich and nontrivial variety of nanostructures including helix and toroid are observed or predicted.[10–17]

One of the main differences of nanostructures of block copolymers confined on the planar (1D) and curved (2D or 3D) substrates is the nature of topological defects.[18,19] The curvature of the substrates imposes a topological requirement on the equilibrium structures with defects. For instance, when the lamellar phase of block copolymers is confined on spherical substrates, requirement of topological constraints should satisfy the Poincaré–Hopf theorem $\sum_i m_i = \chi_E$, where m_i is the charge of the i-th defect and $\chi_E = 2$ is the Euler characteristic of spherical surfaces. One can deduce the minimum number of defects from the equation. The configurations of lamellar phase confined on the spherical surfaces have at least four +1/2 disclination defects or two +1 disclination defects. New experimental techniques to create such a 3D confinement are being rapidly developed.[20–27] Higuchi *et al.* succeeded in preparing various types of complex structures from the diblock copolymers confined in a spherical cavity by a solvent evaporation method.[22] 3D structural analysis reveals that such +1/2 and +1 disclination defects are formed in the surface regions of the spherical cavity. However, it is much more difficult to experimentally grasp universal principles of defect structures due to the fact that precisely controlling the size and shape of the confining environment has not been easily realized so far.

Significant theoretical efforts have been made to understand the defect structures of block copolymers on the flat substrates.[28–30] Nevertheless, theoretical studies regarding the defect structures and ordering kinetics of block copolymers on curved substrates are very challenging, because they require an accurate representation of substrates and the non-linearity is inherent in the continuum model of this system. Currently, theoretical and simulation investigations about the defect structures of block copolymers in the curved space are very limited.[31–36] More recently, Chantawansri and co-workers used a self-consistent field (SCF) theory of inhomogeneous polymers to explore microstructures of block copolymers confined on a

Shanghai Key Laboratory of Advanced Polymeric Materials, State Key Laboratory of Bioreactor Engineering, Key Laboratory for Ultrafine Materials of Ministry of Education, School of Materials Science and Engineering, East China University of Science and Technology, Shanghai 200237, China. E-mail: zhangls@ecust.edu.cn; jlin@ ecust.edu.cn

sphere.[33] Three types of defects of lamellar phase are observed for symmetric diblock copolymers. Isolated disclinations are obtained for the cylindrical phase. Nevertheless, the simulations of SCF theory are limited to the case of small spheres, and cannot capture the defect annihilation of block copolymers confined on spherical substrates. There remains a need for considerable advancements in terms of studying the defect motion of block copolymer nanostructures in the large time scale and thoroughly examining the defect structures.

To address the above challenges, we apply the Landau–Brazovskii (LB) theory to study the self-assembly behaviors of block copolymers confined on spherical substrates. The LB theory of block copolymers can be derived from the many-chain Edwards Hamiltonian following the method of Leibler and Ohta and Kawasaki in the weak segregation limit.[37–39] It has been well established that the LB theory is a convenient way for studying the kinetics of microphase separation of block copolymer systems in the flat space.[40–42] Nevertheless, it has not been implemented in curved spaces. The primary difficulty in extending the LB theory to the spherical geometry is the numerical solution of non-linear partial differential equations. Here, we develop a spectral collocation algorithm with a spherical harmonic basis, which offers high numerical accuracy and efficiency for solving the equations. The spectral method for the spherical geometry is an extension of the spectral method already used in the fluid dynamics.[43]

Beyond developing an improved numerical method for solving the LB theory in curved spaces, we report here on detailed numerical simulations of defect structures and ordering behaviours of both lamellar and cylindrical phases of block copolymers confined on spherical substrates. This new method is able to produce defect structures identified by the Delaunay triangulation, and obtain a relationship between the excess dislocations and the sphere radius which, as far as we know, was not predicted by previous simulations on the self-assembly of block copolymers on a spherical surface. The simulations also directly display the defect annihilation, which cannot be observed by the static SCF simulations. Subsequently, we further investigate the defect structures and ordering behaviours of the lamellar phase. We expect that the present study may offer a rational understanding of the ordering behaviours of nanostructures on curved surfaces and some useful information for the design of novel materials of block copolymers.

2 Theoretical model and numerical method

This section introduces the LB theory and our numerical algorithm for solving it. We consider a thin film of AB diblock copolymers confined on the surface of a sphere with radius R. Here, we assume the thickness h of a thin film satisfying $h \ll R$. The position- and time-dependent order parameter $\varphi(\mathbf{r}, t) \equiv \varphi_A(\mathbf{r}, t) - f_A$ is the deviation of the A segment density $\varphi_A(\mathbf{r}, t)$ from its average value f_A. The scaled LB free energy functional of such a system on the spherical surface s^2 is given by[41,44]

$$F_{s^2}[\varphi] = \int_{s^2} \mathrm{d}\sigma \left\{ \frac{1}{2}\left[\left(1 + \nabla_{s^2}{}^2\right)\varphi\right]^2 + \frac{\varepsilon}{2}\varphi^2 - \frac{s}{3!}\varphi^3 + \frac{1}{4!}\varphi^4 \right\} \quad (1)$$

where $\mathrm{d}\sigma$ is the infinitesimal element of the area and $\nabla_{s^2}{}^2$ corresponds to the spherical Laplacian operator. The parameter ε is a temperature-like variable, which is related to the Flory–Huggins interaction parameter. The variable s is related to the composition asymmetry of copolymers, and vanishes at $f_A = 0.5$. The specific relationships of the above parameters with the composition, polymerization degree and Flory–Huggins interaction parameter are given in ref. 41 and 45. The phase diagram obtained from the one-mode or two-mode approximation is sketched in ref. 44. Since the order parameter φ is a conserved variable, its dynamics satisfies the following Cahn–Hilliard equation, which is also known as Model B in condensed matter physics[46]

$$\frac{\partial \varphi}{\partial t} = \nabla_{s^2}{}^2 \frac{\delta F_{s^2}}{\delta \varphi} + \zeta \quad (2)$$

where $\delta F_{s^2}/\delta\varphi$ denotes the functional derivative of the free energy functional with respect to φ, and ζ stands for a conserved noise satisfying the fluctuation–dissipation theorem.

Next, the numerical approach to solve the non-linear partial differential equation in the curved space is stated. Rather than using the finite element or finite volume methods, we extend a highly accurate spectral method to solve eqn (2). In the flat Euclidian space, an attractive way to solve the non-linear partial differential equations with the periodic boundary conditions is the Fourier spectral method.[43] Similarly, in the case of the spherical geometry with fixed radius R, the basis of spherical harmonics is chosen, which involves the back and forth transformations between the real- and spectral-space representations. In the real space, the order parameter field $\varphi(\mathbf{r})$ is represented by the spherical-polar coordinate $\mathbf{u}(\varphi, \theta)$, where $\varphi \in [0, 2\pi]$ denotes the longitude and $\theta \in [-\pi/2, \pi/2]$ denotes the latitude. The spherical harmonic expansion is defined by[47]

$$\varphi(r) \equiv \varphi(\mathbf{u}) = \sum_{l=0}^{\infty} \sum_{m=-l}^{m=l} \tilde{\varphi}_l^m Y_l^m(\mathbf{u}) \quad (3)$$

where $Y_l^m(\mathbf{u})$ denotes the spherical harmonic of degree l for $-l \le m \le l$ and $\tilde{\varphi}_l^m$ is the component of $\varphi(\mathbf{u})$ in the spherical-harmonic space. Since the spherical harmonics are the eigenfunctions of the spherical Laplacian operator, one can calculate the Laplacian of $\varphi(\mathbf{u})$ *via* application of the operator termwise in the expansion of eqn (3), which is given by $\nabla_{s^2}{}^2\varphi(\mathbf{u}) = \sum_{l=0}^{\infty} \sum_{m=-l}^{m=l} -\frac{l(l+1)}{R^2} \tilde{\varphi}_l^m Y_l^m(\mathbf{u})$. With this, the evolution equation (eqn (2)) of the order parameter field can be re-expressed in the spherical-harmonic space

$$\frac{\partial \tilde{\varphi}_l^m}{\partial t} = -\frac{l(l+1)}{R^2}\left[\left(\left(1 - \frac{l(l+1)}{R^2}\right)^2 + \varepsilon\right)\tilde{\varphi}_l^m + \widetilde{NL}_l^m\right] \quad (4)$$

Here, $\widetilde{NL}_l^m$ is the component of nonlinear term $-s\frac{\varphi^2(\mathbf{u})}{2} + \frac{\varphi^3(\mathbf{u})}{3!}$ in the spherical-harmonic space. The conserved noise term of eqn (2) is neglected in the spectral

method for the sake of numerical simplification. The above equations for the order parameter field $\tilde{\varphi}_l^m$ are numerically solved by a semi-implicit scheme in the equally spaced grid.[48] The back and forth transformations between the real space and spherical-harmonic space are performed by using the SPHEREPACK 3.2 software package.[49]

In our simulations, the initial configurations are the disordered states, in which uniform random numbers between -0.1 and 0.1 are assigned to the order parameter field at the lattice sites of the spherical surface. To ensure that the observed defect structures are not accidental, we repeat the simulations 10 times using different initial random configurations. Usually, the initial configurations quickly evolve into ordered structures. However, for a quenching system with a large sphere radius, the configurations still contain lots of defects even after a long-time run due to a kinetically slow process of defect annihilation. To promote the escape of metastable configurations, an annealing process is subsequently performed. Specifically, the initial configurations of the annealing process are the final states of quenching simulations. The parameter ε linearly increased with the simulation step, but remained below the critical value of the disorder-to-order transition, and then linearly decreased to the initial setting value ε_0. The above procedure is cycled 6–10 times until the total energy of the system with ε_0 at different cycles does not change. The annealing process used in our simulations may correspond to the multi-cycle annealing process in the experiments, which has been applied to prepare highly aligned patterns of block copolymers in the Harrison *et al.* study.[28]

3 Results and discussion

In contrast to the microphase separation of block copolymers in the flat space, the nanostructures of block copolymers confined on the spherical substrates depend not only on the parameters ε_0 and s, but also on the curvature of the sphere. The topology of the sphere enforces a requirement of defect structures in the equilibrium configurations. In what following, we investigate the defects and ordering processes of both cylindrical and lamellar phases of diblock copolymers confined on the surfaces of spheres with different radii.

3.1 Defect structures and ordering behaviours of the cylindrical phase

In this subsection, we choose the parameters $\varepsilon_0 = -0.13$ and $s = 0.3$, which correspond to the case of asymmetric block copolymers. The cylindrical phase is stable.[44] In order to determine the defect structures of the cylindrical phase on the spherical surfaces, two main steps are performed during the standard data post-processing. In the first step, the cores or vertices of cylinder domains are determined through the local maxima of the order parameter field. In the second step, the algorithm of Delaunay triangulation with these vertices in the curved space is conducted.[50] It is useful to visualize the defect structures through diagrams shown in Fig. 1(b) and 2(b), which are constructed by lines connecting a vertex (represented by a small sphere) with all of its neighbours. The number of lines of a vertex is used to identify the defect type. The five-fold and seven-fold coordinated vertices can be respectively characterized by the disclination charges +1 and −1, which are the departure of the coordination number from the flat space value of 6. A tightly bound pair of +1 and −1 disclinations forms a dislocation.

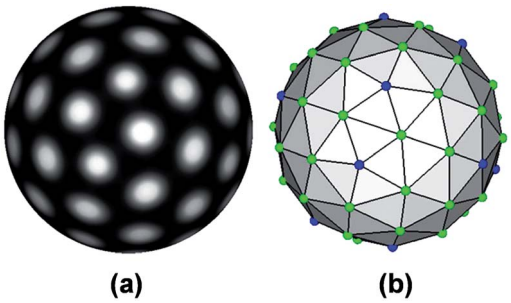

Fig. 1 (a) Profile of the order parameter field for 60 cylinder domains on the surface of a sphere with radius $R \approx 2.0a$ (a is the mean distance of cylinder pairs). White and gray colors refer to large and small values of the order parameter field, respectively. (b) Associated diagram of Delaunay triangulation for the cylinders or vertices on the spherical surface. The vertices symbolled by the small spheres denote the centres of cylinder domains. Five-fold, six-fold and seven-fold coordinated vertices are colored by blue, green and red, respectively. The solid lines represent the connections of a vertex with its neighbours.

Defect structures of the cylindrical phase. Fig. 1(a) shows the profile of the order parameter field on the surface of a sphere with radius $R \approx 2.0a$, where a is the average distance of the cylinder pairs. The order parameter field on the closed surface is represented as a gray-white field, where the gray and white colors correspond to the small and large values of the order parameter field, respectively. This configuration contains 60 cylinders arranged on the spherical substrate. The associated diagram of Delaunay triangulation is illustrated in Fig. 1(b). The vertices correspond to the local maxima of the order parameter. 12 isolated +1 disclinations (five-fold coordinated sites) are observed in the Delaunay diagram. In the flat space, the isolated

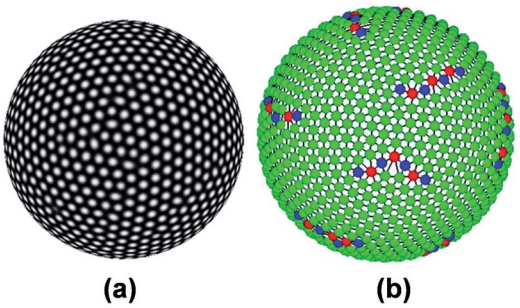

Fig. 2 (a) Profile of the order parameter field for 1052 cylinder domains on the surface of a sphere with radius $R \approx 8.20a$. (b) Associated diagram of Delaunay triangulation for the cylinders or vertices on the spherical surface. The representations of colors, symbols and lines are the same as shown in Fig. 1. The small spheres with red color denote the vertices with seven-fold coordinated sites.

+1 disclinations are not usually found because they produce large distortions in the configuration. In contrast, on the curved substrates, the disclinations help to screen out the geometric frustration to reduce the distortions.[19] In the multi-cycle annealing process, the isolated +1 disclinations cannot be removed away. This phenomenon manifests the fact that the isolated +1 disclinations are an intrinsic part of the configurations on the spherical substrates.

As the total number of cylinder domains or sphere radius increases, dislocations are introduced into the system to further reduce the distortions of isolated +1 disclinations. For instance, the system with sphere radius $R \approx 8.20a$ is quenched from the random initial configuration, and the annealing process is subsequently performed. As shown in Fig. 2(a), the cylinders are arranged on the spherical surface, and the final configuration of the order parameter field consists of 1052 cylinders. Fig. 2(b) shows the associated diagram of Delaunay triangulation, which contains 51 five-fold, 962 six-fold and 39 seven-fold coordinated sites. The isolated +1 or −1 disclinations are not observed in the final configuration. One can observe that pairs of +1 and −1 disclinations produce chains of dislocations. Note that a chain of 5–7 pair dislocations arranged around an unpaired +1 disclination, *i.e.*, 5–7–5–7–5–7–5, is illustrated in Fig. 2(b). The defect structures are called scars, which are experimentally observed in the spherical crystals.[51] Here, the number of excess dislocations in a scar has a value of 3. It should be mentioned that the scars cannot be further annihilated in the annealing simulations, suggesting that the scar structures are an intrinsic part of configurations on the spherical surfaces.

To quantify the behaviours of the scars, we determine the mean number of excess dislocations in a scar from the diagram of Delaunay triangulation, and plot the result as a function of the relative sphere radius R/a, which is displayed in Fig. 3. Each data point is collected from ten independent runs. Below the critical value of the relative sphere radius $(R/a)_c \approx 5.0$, only 12 isolated +1 disclinations are observed, and the dislocations cannot be produced in this system. As the sphere radius increases, the isolated disclinations become much more energetically cost, while the formation of dislocation chains may reduce the energy. Above the critical value of $(R/a)_c$, the mean number of excess dislocations in a scar increases with the relative sphere radius. In the range of large sphere radii, the number of excess dislocations in a scar grows proportional to the relative sphere radius, and the obtained best-fit slope is 0.435. Since the different initial states result in the metastable configurations with different amounts of excess dislocations in a scar, the non-integer number of dislocation appears in Fig. 3 due to the averaging of several runs.

Ordering behaviours of the cylindrical phase. Upon quenching the system below the critical value of the disorder-to-order transition, the initial configurations with small random fluctuations evolve into ordered patterns. To characterize the order degree of cylinder nanostructures, we calculate the defect fraction to monitor the ordering dynamics. The defect fraction at time t is defined as $\mathrm{DF}(t) = (N - V_6)/N \times 100\%$,[52,53] where V_6 and N are the number of six-fold coordinated vertices and the total number of vertices in the diagram of Delaunay triangulation, respectively. Here, we do not distinguish the defects with five-fold (+1), seven-fold (−1), or other coordinated sites, and only the total defects are collected from the diagram of Delaunay triangulation. The typical temporal evolution of the defect fraction is shown in Fig. 4. From the double-logarithmic plot, one can see that there are two stages in the ordering process of the cylindrical phase on the spherical surfaces. The defect fraction as a function of time t obeys the power law $\mathrm{DF}(t) \propto t^{-1/3}$ for the time from 0 to $10^2\tau$, and $\mathrm{DF}(t) \propto t^{-1/5}$ for the time from $10^2\tau$ to $10^3\tau$. Here, τ is the time unit in simulations. At the early stage of the ordering process, the spherical substrate cannot affect the kinetic behaviour, which obeys the evaporation–condensation mechanism derived by Lifshitz and Slyozov in the

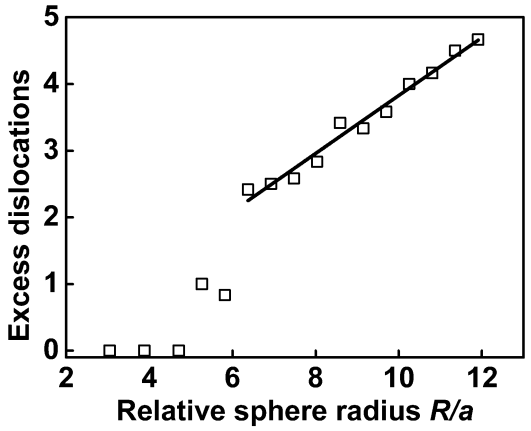

Fig. 3 Mean number of excess dislocations in a scar as a function of relative sphere radius R/a. All the data points represent the average value of ten samples. The solid line is the best-fit curve in the range of large spherical radii, and the obtained slope is 0.435.

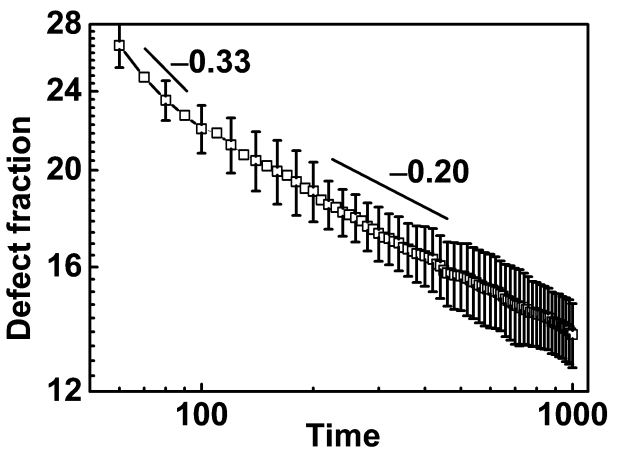

Fig. 4 Typical time evolution of the defect fraction of the cylindrical phase on the spherical surface during the quenching simulation. The defect fraction at time t is defined as $\mathrm{DF}(t) = (N - V_6)/N \times 100\%$, where V_6 and N are the number of six-fold coordinated vertices and the total number of vertices in the diagram of Delaunay triangulation, respectively. Each data point is collected from ten independent runs. The error bars are successively skipped one point for the sake of clarity. Two solid lines represent the best-fit power laws in the range of early and intermediate stages of the ordering process.

flat space.[54] As time proceeds, the decay of the defect fraction is slower than that of the early stage, and the defect annihilation is strongly affected by the geometrical characteristics of the substrates. It should be mentioned that the sphere radius can affect the transition time of the scaling law in the quenching simulations.

At the late stage of simulations, the total number of cylinder domains does not further change, but the scars are generated by the local motion of disclinations and dislocations. Fig. 5 shows the formation of a scar on the spherical surface at the late stage of quenching simulation. Snapshots (a) and (d) are the initial and final configurations of scar formation within the highlighted area, respectively. For the sake of clarity, snapshots (b) and (c) display a portion of configurations. In the bottom of the highlighted area, there is a high-angle grain boundary, as shown in Fig. 5(a). The near +1 disclinations are unstable, and start to locally re-arrange. A new 5–7 pair dislocation is generated (Fig. 5(b)). Subsequently, the new dislocation glides towards the nearest isolated +1 disclination, and quickly forms a mini-scar (5–7–5 grain boundary), which is illustrated in Fig. 5(c). Eventually, the mini-scar further joins the nearest 5–7 pair dislocation to generate a 5–7–5–7–5 scar (Fig. 5(d)).

The formation of scars on the spherical surfaces is similar to that reported in the experimental and theoretical studies of Bowick *et al.*[55,56] In their studies, one colloid is added to or subtracted from the initial structures of spherical crystals. The curvature of the sphere drives the formation of dislocations. The individual dislocation then glides towards the nearest isolated disclination. The dislocation binding with the disclination forms 5–7–5 mini-scar. As shown in Fig. 5(b) to (d), the formation of scars from isolated +1 disclinations *via* mini-scars is observed. The process of scar formation is in general agreement with the findings of Bowick *et al.*

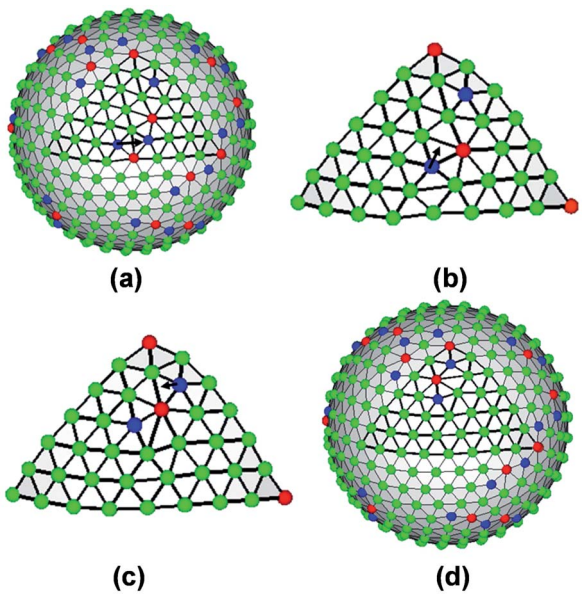

Fig. 5 Typical formation process of a scar within the highlighted area. Time: (a) $\Delta t/\tau = 0$, (b) $\Delta t/\tau = 35$, (c) $\Delta t/\tau = 90$, and (d) $\Delta t/\tau = 155$. Here, τ is the time unit in simulations. Snapshot (a) displays the initial configuration from the quenching simulation, while snapshot (d) displays the configuration where a scar is formed within the highlighted area. For the sake of clarity, only one portion of the diagram of Delaunay triangulation is drawn in snapshots (b) and (c). The representations of colors, symbols and lines are the same as shown in Fig. 1. The arrows indicate the motion directions of vertices.

We wish to emphasize that although the LB theory of block copolymers can predict the scar structures and scar formation, there exists a significant difference between the block copolymers and colloids confined on the spherical surfaces. In the system of colloids, the shape and size of colloids are not perturbed by the strain field of defects, and the number of colloids is fixed in the particle motion. However, the polymer chains can stretch to change the shape of the cylinder domains due to the strain field introduced by the disclinations, and the coalescence of cylinder domains may take place in the evolution. These result in the fact that the number of cylinder domains is not a conserved variable. Therefore, for the system of colloids, the kinetic behaviors of defect structures may experience some degree of variations.

3.2 Defect structures and ordering behaviours of the lamellar phase

In this subsection, we turn to investigate the lamellar phase of symmetric block copolymers confined on the spherical substrates. The parameters are set as $\varepsilon_0 = -0.2$ and $s = 0.0$.[44] The system size is characterized by the ratio $2\pi R/d$, where R is the sphere radius and d is the average repeat spacing of lamellae. In the present work, because of the difficulty in the automated recognition algorithm of defect structures of the lamellar configuration in the curved space, we only concentrate on the defect structures and the ordering process of the lamellar phase on the spherical surfaces.

Defect structures of the lamellar phase. The lamellar phase is analogous to the smectic-A liquid crystals. Here, we use the type of defect of liquid crystals to characterize the defect structures of the lamellar phase. The +1/2 and +1 disclinations are illustrated in Fig. 6. More details about the defects of liquid crystals can be found in the monograph of de Gennes and Prost.[57]

Fig. 6 summarizes the obtained defect structures of the lamellar phase on the surface of a sphere with a small radius in the multi-cycle annealing simulations. The left column in Fig. 6 displays the profiles of the order parameter field on the spherical surfaces. To gain a better view of the corresponding configuration on the spherical surface, we also plot the modified Mercator projections, which are illustrated in the right column of Fig. 6. The horizontal and vertical axes respectively refer to the $x = R\varphi$ and $y = \frac{5}{4}R\ln\left(\tan\left(\frac{\pi}{4} + \frac{2}{5}\theta\right)\right)$, where $\varphi \in [0, 2\pi]$ denotes the longitude and $\theta \in [-\pi/2, \pi/2]$ denotes the latitude. Here, the defect structures of the lamellar phase on the spherical substrates could be empirically classified into three categories.[33] The first class is the quasi-baseball defect structure, as shown in Fig. 6(a). Four +1/2 disclinations denoted by the red circle symbols are equally spaced at 90° intervals on a great circle. The quasi-baseball structure contains more than

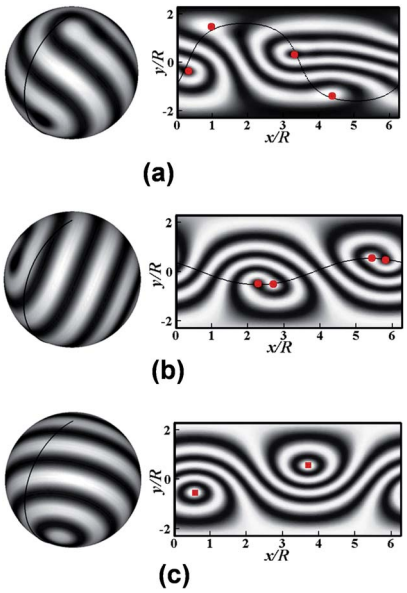

Fig. 6 Defect structures of the lamellar phase confined on the spherical substrates. (a) System size $2\pi R/d \approx 10.0$, quasi-baseball defect structure; (b) system size $2\pi R/d \approx 11.0$, spiral defect structure; and (c) system size $2\pi R/d \approx 12.0$, hedgehog defect structure. White (gray) color refers to large (small) values of the order parameter field. Left column shows the profiles of the order parameter field on the spherical surfaces. The curve on the spherical surface denotes the longitude $\varphi = 0$ and the range of latitudes $\theta \in [-\pi/2, \pi/2]$. Right column is the modified Mercator projections of the order parameter field. The horizontal and vertical axes respectively refer to the $x = R\varphi$ and $y = \frac{5}{4}R \ln\left(\tan\left(\frac{\pi}{4} + \frac{2}{5}\theta\right)\right)$, where $\varphi \in [0, 2\pi]$ denotes the longitude and $\theta \in [-\pi/2, \pi/2]$ denotes the latitude. The red circles and squares represent the cores of +1/2 and +1 disclinations, respectively. The curve in the projection represents a great circle passing through the defect cores.

two stripes. The strip termination can appear at the core of each disclination. The second class, as illustrated in Fig. 6(b), is called the spiral defect structure. The structure has the same number of disclinations as the quasi-baseball structure. However, the four +1/2 disclinations are not evenly spaced. The spiral structure contains only two continuous stripes. The stripes are spirals around the cores of disclinations, and terminate at the centre of other disclinations. The third class is called the hedgehog defect structure, as observed in Fig. 6(c). All stripes are circularly arranged on the spherical surface, and there are two +1 disclinations at the two opposite positions of the sphere. It should be noted that Chantawansri *et al.* developed a self-consistent field theory in the spherical geometry to investigate the defect structures of the lamellar phase of block copolymers.[33] The defect structures including hedgehog, quasi-baseball and spiral are predicted in their calculations. Furthermore, by quantitatively analysing the free energy density of the structures, they found that the quasi-baseball defect structure is metastable, and its energy is close to that of the spiral defect structure.

It is difficult at this time to make a comprehensive comparison between the theoretical predictions and experimental observations due to limited experimental studies on self-assembly behaviours of block copolymers confined on the spherical substrates. However, we can still compare the calculation results with some existing studies. For example, Higuchi *et al.* reported microphase-separated structures of polystyrene-*block*-polyisoprene (PS-*b*-PI) by a 3D confinement.[22] A 3D reconstructed technique is used to identify the nanostructures of block copolymers. They found that the complex structures are only formed in the surface region of the sphere cavity. Ring structures of the PS phase and the PI phase are arranged at the spherical surface. Another type of morphology is the "helix" structure, where the PS phase twists around the PI phase. According to the simulation results, when the symmetric block copolymers are confined on the spherical surfaces, the lamellae are circularly arranged on the spherical surface (Fig. 6(c)), which corresponds to the ring structure in the experiment. As shown in Fig. 6(b), two continuous lamellae mutually twist. This structure is very similar to the "helix" structure in the experiment.

Ordering behaviours of the lamellar phase. Fig. 7 shows the evolution of the lamellar phase confined on the surface of a sphere with a large radius after quenching from the

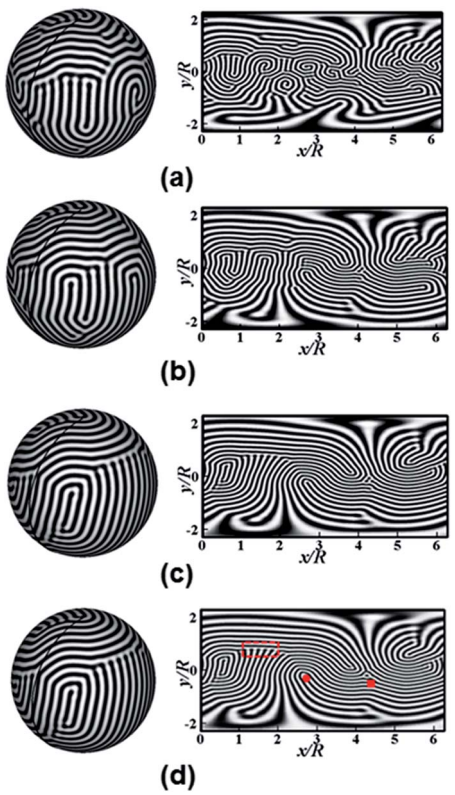

Fig. 7 Snapshots of the ordering process of the lamellar phase in the quenching simulation. Time: (a) $t/\tau = 300$, (b) $t/\tau = 5000$, (c) $t/\tau = 28\,000$, and (d) $t/\tau = 50\,000$. Left column shows the profiles of the order parameter field on the surface of a sphere with $2\pi R/d \approx 51.0$. Right column is the modified Mercator projections of the order parameter field. The representations are the same as shown in Fig. 6. In panel (d), the red circle and square denote respectively the cores of disclination and dislocation, and the dashed box encloses the grain boundary.

homogenous state. Due to the disordered initial configuration, randomly distributed lamellae are observed at the early time (Fig. 7(a)). The poor orientation lamellae locally re-arrange to form the highly aligned lamellae, and the dislocations and multi-poles of disclinations are annihilated by the motion of defects. The facts result in an increase of order degree of lamellar configuration at the intermediate stage (Fig. 7(b) and (c)). In the quenching simulation of the system with a large sphere radius, the resulting configuration is usually the "polycrystalline" state with randomly oriented lamellae. Fig. 7(d) illustrates the final configuration of lamellae on the surface of a sphere with radius $2\pi R/d \approx 51.0$. The characteristic of such a configuration is the presence of a large amount of defects, such as grain boundaries, dislocations and disclinations, which are also highlighted in Fig. 7(d). Comparison between the configurations of different times $t = 2.8 \times 10^4\tau$ (Fig. 7(c)) and $t = 5.0 \times 10^4\tau$ (Fig. 7(d)) indicates that the evolution of the order parameter field cannot further annihilate the defects, and the configuration remains practically constant beyond $t = 5.0 \times 10^4\tau$ in the quenching simulation.

A typical example of defect annihilation on the spherical substrate is illustrated in Fig. 8. A portion of the lamellar configuration is extracted from the profile of the order parameter field on the spherical surface. Panel (a) shows a disclination dipole with the +1/2 and −1/2 disclination cores, and a grain boundary evolving from a disclination dipole. The spacing between them is widely separated. The high strain energy of the disclination dipole causes the defects to evolve. The fact gives rise to production of a grain boundary, as observed in the left of panel (b). Subsequently, this defect structure climbs normal to the boundary, and the defect motion reduces the separation distance of defect pairs, which is illustrated in panel (c). The disclination dipole in the bottom right of panel (c) is the result of defect motion, which is out of the portion of the lamellar configuration. Finally in panel (d), the disclination dipole and grain boundary are annihilated by the local motion of defects to reduce the strain energy, and only a dislocation remains in the panel.

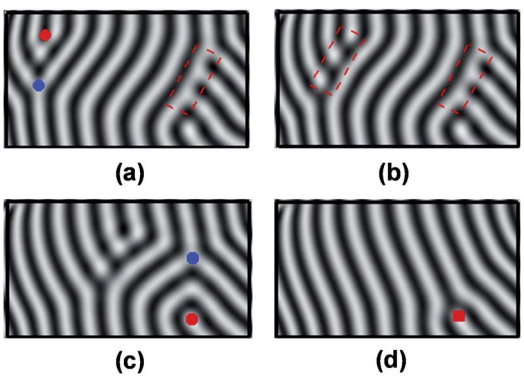

Fig. 8 Snapshots of defect annihilation. (a) $\Delta t/\tau = 0$, the spacing between the disclination dipole and the grain boundary is widely separated. (b) $\Delta t/\tau = 4600$, the dipole of disclinations evolves into a grain boundary. (c) $\Delta t/\tau = 5900$, the spacing between the defects decreases. (d) $\Delta t/\tau = 6200$, the number of defects decreased, but a dislocation still exists in the bottom right. The panels are only a portion of the lamellar phase on the spherical surface. The cores of +1/2 disclinations, −1/2 disclinations and dislocation are indicated by the red circles, blue circles and red square, respectively. The grain boundaries are enclosed by the dashed boxes.

The type of defect annihilation described above is the main mechanism of the ordering process of the lamellar phase on the spherical surfaces for the set of parameters chosen in this study. It is very similar to the defect annihilation identified by Harrison *et al.* on the flat substrates. Harrison *et al.* studied the ordering dynamics of the lamellar phase of block copolymers in a thin film.[28] The results reveal that the annihilation of quadrupole consisting of two disclination pairs is the dominant mechanism of the ordering process. Like Harrison's study, the process of defect annihilation in our simulations involves the disclinations and grain boundaries. As shown in Fig. 8, the grain boundary evolves from the disclination dipole, and re-organizes into a disclination dipole due to the defect motion. Thus, the ordering mechanism in our simulations is very similar to that reported in the experimental findings by Harrison *et al.* It should be mentioned that the annihilation of dislocations is not frequently observed due to the small size of the system in our simulations.

Unlike the intrinsic defects on the spherical surfaces (Fig. 6), the defects of the lamellar phase on the surface of a large sphere can be further annihilated by the annealing simulation. Fig. 9 shows the ordering process of the lamellar phase in the subsequent annealing process. The initial state is the configuration with defects of grain boundaries, dislocations and disclinations (Fig. 7(d)). After several cycles of the annealing process, the defects of the lamellar configuration are gradually annihilated, and the lamellar patterns with highly aligned order on the spherical surface are observed in Fig. 9(a). After sufficient cycles of the annealing process, the well-aligned lamellae dominate the spherical surface (Fig. 9(b)). However, the four +1/2 disclinations located on a great circle still exist on the spherical surface. The nearest cores of disclinations are separated by about 4 stripes. According to the classification of defects, the defect structure of this lamellar configuration is spiral.

Although the LB model and spectral method presented here provide a powerful methodology for studying the defect structures and ordering behaviours of block copolymers on the

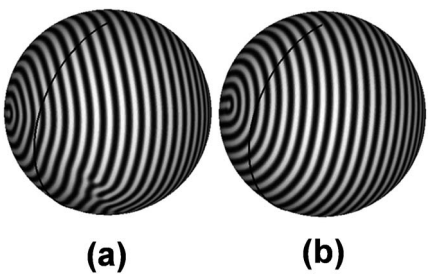

Fig. 9 Snapshots of the ordering process in the annealing process. The initial state is the configuration of Fig. 7(d). (a) Configuration after 6 cycles of the annealing process and (b) configuration after 10 cycles of the annealing process.

spherical substrates, there are still some drawbacks for the cases of tackling the complex systems or geometries. Here, a few comments on the model and numerical method are in order. First of all, for complex systems containing block copolymers, there are certainly some opportunities to improve the model. For instance, the free energy functional used in the model is a simplified form of density functional theories in the weak segregation limit, and does not explicitly take into account the conformational entropy of polymer chains. To solve this problem, one can replace eqn (1) with a free energy form of coarse-grained microscopic model, *e.g.*, self-consistent mean-field theory of inhomogeneous polymers, which accounts for the chain connectivity and provides a unified treatment of polymer systems from the weak to strong segregation regions.[58] With these improvements, one can accurately calculate the free energy of different structures, and distinguish the metastable configurations of spiral and quasi-baseball defects on spherical substrates.

Secondly, the surface topology in our present study is the spherical geometry, and a spherical harmonic basis is adopted to numerically solve the model equations. It is difficult to extend the numerical method used in our simulations to more complex geometries ranging from ellipsoids to cylinders and spheres with a bump. To overcome the drawback, Marenduzzo *et al.* recently proposed a modified finite element algorithm to discrete the Laplace–Beltrami operator and non-linear terms of the free energy.[59] They applied the algorithm to tackle the problems of phase separation dynamics on the non-spherical surfaces. It is possible to extend the finite element scheme to solve the equations of the LB model or self-consistent field theory of polymers, and to investigate the defect structures and dynamics behaviours of block copolymers on the complex geometries, such as the negative-curvature surfaces.

4 Conclusions

In summary, the LB model of block copolymers, which is numerically solved by the spectral method with a spherical harmonic basis, is used to investigate the defect structures and ordering dynamics of both cylindrical and lamellar phases on the spherical substrates. For the cylindrical phase, the isolated disclinations emerge in the system with a small sphere radius. The scars are formed on the surface of a sphere with a large radius, and the number of excess dislocations in a scar is linearly proportional to the sphere radius. The defect fraction of the cylindrical phase exponentially decays, and the formation of scars from isolated disclinations *via* mini-scars was observed. For the lamellar phase, the defect structures of hedgehog, spiral and quasi-baseball are produced on spherical substrates, and the disclination annihilation is the dominant ordering mechanism of the lamellar phase.

Acknowledgements

This work was supported by the National Natural Science Foundation of China (51203049, 21234002), and Research Fund for the Doctoral Program of Higher Education of China (20120074120003).

Notes and references

1 M. W. Matsen and M. Schick, *Phys. Rev. Lett.*, 1994, **72**, 2660.
2 E. W. Cochran, C. J. Garcia-Cervera and G. H. Fredrickson, *Macromolecules*, 2006, **39**, 2449.
3 M. Park, C. Harrison, P. M. Chaikin, R. A. Register and D. H. Adamson, *Science*, 1997, **276**, 1401.
4 A. M. Jackson, J. W. Myerson and F. Stellacci, *Nat. Mater.*, 2004, **3**, 330.
5 C. Park, J. Yoon and E. L. Thomas, *Polymer*, 2003, **44**, 6725.
6 P. Broz, S. Driamov, J. Ziegler, N. Ben-Haim, S. Marsch, W. Meier and P. Hunziker, *Nano Lett.*, 2006, **6**, 2349.
7 H. P. Huinink, M. A. van Dijk, J. C. M. Brokken-Zijp and G. J. A. Sevink, *Macromolecules*, 2001, **34**, 5325.
8 Q. Wang, P. F. Nealey and J. J. de Pablo, *Macromolecules*, 2001, **34**, 3458.
9 A. Knoll, A. Horvat, K. S. Lyakhova, G. Krausch, G. J. A. Sevink, A. V. Zvelindovsky and R. Magerle, *Phys. Rev. Lett.*, 2002, **89**, 035501.
10 Y. Wu, G. Cheng, K. Katsov, S. W. Sides, J. Wang, J. Tang, G. H. Fredrickson, M. Moskovits and G. D. Stucky, *Nat. Mater.*, 2004, **3**, 816.
11 H. Xiang, K. Shin, T. Kim, S. Moon, T. J. McCarthy and T. P. Russell, *J. Polym. Sci., Part B: Polym. Phys.*, 2005, **43**, 3377.
12 W. Li, R. A. Wickham and R. A. Garbary, *Macromolecules*, 2006, **39**, 806.
13 P. Chen, X. He and H. Liang, *J. Chem. Phys.*, 2006, **124**, 104906.
14 B. Yu, P. Sun, T. Chen, Q. Jin, D. Ding, B. Li and A.-C. Shi, *Phys. Rev. Lett.*, 2006, **96**, 138306.
15 J. G. E. M. Fraaije and G. J. A. Sevink, *Macromolecules*, 2003, **36**, 7891.
16 B. Yu, B. Li, Q. Jin, D. Ding and A.-C. Shi, *Soft Matter*, 2011, **7**, 10227.
17 C. R. Stewart-Sloan and E. L. Thomas, *Eur. Polym. J.*, 2011, **47**, 630.
18 D. R. Nelson, *Nano Lett.*, 2002, **2**, 1125.
19 P. Chaikin and T. Lubensky, *Principles of Condensed Matter Physics*, Cambridge University Press, 1995.
20 H. Yabu, T. Higuchi and M. Shimomura, *Adv. Mater.*, 2005, **17**, 2062.
21 T. Higuchi, A. Tajima, K. Motoyoshi, H. Yabu and M. Shimomura, *Angew. Chem., Int. Ed.*, 2008, **47**, 8044.
22 T. Higuchi, K. Motoyoshi, H. Sugimori, H. Jinnai, H. Yabu and M. Shimomura, *Soft Matter*, 2012, **8**, 3791.
23 N. Saito, R. Takekoh, R. Nakatsuru and M. Okubo, *Langmuir*, 2007, **23**, 5978.
24 S. J. Jeon, G. R. Yi, C. M. Koo and S. M. Yang, *Macromolecules*, 2007, **40**, 8430.
25 S. J. Jeon, G. R. Yi and S. M. Yang, *Adv. Mater.*, 2008, **20**, 4103.
26 D. A. Rider, J. I. L. Chen, J.-C. Eloi, A. C. Arsenault, T. P. Russell, G. A. Ozin and I. Manners, *Macromolecules*, 2008, **41**, 2250.

27 S. G. Jang, D. J. Audus, D. Klinger, D. V. Krogstad, B. J. Kim, A. Cameron, S.-W. Kim, K. T. Delaney, S.-M. Hur, K. L. Killops, G. H. Fredrickson, E. J. Kramer and C. J. Hawker, *J. Am. Chem. Soc.*, 2013, **135**, 6649.
28 C. Harrison, H. Adamson, Z. Cheng, J. M. Sebastian, S. Sethuraman, D. A. Huse, R. A. Register and P. M. Chaikin, *Science*, 2000, **290**, 1558.
29 D. A. Vega, C. K. Harrison, D. E. Angelescu, M. L. Trawick, D. A. Huse, P. M. Chaikin and R. A. Register, *Phys. Rev. E: Stat., Nonlinear, Soft Matter Phys.*, 2005, **71**, 061803.
30 R. A. Segalman, A. Hexemer, R. C. Hayward and E. J. Kramer, *Macromolecules*, 2003, **36**, 3272.
31 P. Tang, F. Qiu, H. Zhang and Y. Yang, *Phys. Rev. E: Stat., Nonlinear, Soft Matter Phys.*, 2005, **72**, 016710.
32 J. F. Li, J. Fan, H. D. Zhang, F. Qiu, P. Tang and Y. Yang, *Eur. Phys. J. E*, 2006, **20**, 449.
33 T. L. Chantawansri, A. W. Bosse, A. Hexemer, H. D. Ceniceros, C. J. Garcia-Cervera, E. J. Kramer and G. H. Fredrickson, *Phys. Rev. E: Stat., Nonlinear, Soft Matter Phys.*, 2007, **75**, 031802.
34 B. Vorselaars, J. U. Kim, T. L. Chantawansri, G. H. Fredrickson and M. W. Matsen, *Soft Matter*, 2011, **7**, 5128.
35 L. R. Gómez and D. A. Vega, *Phys. Rev. E: Stat., Nonlinear, Soft Matter Phys.*, 2009, **79**, 031701.
36 M. Pinna, S. Hiltl, X. Guo, A. Böker and A. V. Zvelindosky, *ACS Nano*, 2010, **4**, 2845.
37 S. A. Brazovskii, *J. Exp. Theor. Phys.*, 1975, **41**, 85.
38 L. Leibler, *Macromolecules*, 1980, **13**, 1602.
39 T. Ohta and K. Kawasaki, *Macromolecules*, 1986, **19**, 2621.
40 S. Qi and Z.-G. Wang, *Phys. Rev. Lett.*, 1996, **76**, 1679.
41 R. A. Wickham and A.-C. Shi, *J. Chem. Phys.*, 2003, **118**, 10293.
42 M. Pinna and A. V. Zvelindovsky, *Eur. Phys. J. B*, 2012, **85**, 210.
43 C. Canuto, M. Y. Hussaini, A. Quarteroni and T. A. Zang, *Spectral Methods in Fluid Dynamics*, Springer, 1988.
44 I. W. Hamley and V. E. Podneks, *Macromolecules*, 1997, **30**, 3701.
45 G. H. Fredrickson and E. Helfand, *J. Chem. Phys.*, 1987, **87**, 697.
46 P. C. Hohenberg and B. I. Halperin, *Rev. Modern Phys.*, 1977, **49**, 435.
47 G. B. Arfken and H. J. Weber, *Mathematical Methods for Physicists: A Comprehensive Guide*, Academic Press, 6th edn, 2005.
48 W. Press, S. Teukolsky, W. Vetterling and B. Flannery, *Numerical Recipes in Fortran: the Art of Scientific Computing*, Cornell University Press, 1992.
49 J. C. Adams and P. N. Swarztrauber, *Mon. Weather Rev.*, 1999, **127**, 1872.
50 R. J. Renka, *ACM Trans. Math. Software*, 1997, **23**, 416.
51 R. Bausch, M. J. Bowick, A. Cacciuto, A. D. Dinsmore, M. F. Hsu, D. R. Nelson, M. G. Nikolaides, A. Travesset and D. A. Weitz, *Science*, 2003, **299**, 1716.
52 Y. Yokojima and Y. Shiwa, *Phys. Rev. E: Stat., Nonlinear, Soft Matter Phys.*, 2002, **65**, 056308.
53 H. Qian and G. F. Mazenko, *Phys. Rev. E: Stat., Nonlinear, Soft Matter Phys.*, 2003, **67**, 036102.
54 M. Lifshitz and V. V. Slyozov, *J. Phys. Chem. Solids*, 1961, **19**, 35.
55 P. Lipowsky, M. J. Bowick, J. H. Meinke, D. R. Nelson and A. R. Bausch, *Nat. Mater.*, 2005, **4**, 407.
56 M. Bowick, A. Cacciuto, D. R. Nelson and A. Travesset, *Phys. Rev. Lett.*, 2002, **89**, 185502.
57 P. G. de Gennes and J. Prost, *The Physics of Liquid Crystals*, Oxford University Press, 2nd edn, 1993.
58 G. H. Fredrickson, *The Equilibrium Theory of Inhomogeneous Polymers*, Oxford University Press, 2006.
59 D. Marenduzzo and E. Orlandini, *Soft Matter*, 2013, **9**, 1178.